Temperature oscillations in turbulent Rayleigh-Bénard convection

X.-L. Qiu and P. Tong*
Department of Physics, Oklahoma State University, Stillwater, Oklahoma 74078
(Received 5 March 2002; revised manuscript received 20 March 2002; published 23 August 2002)

A systematic study of temperature oscillations in turbulent thermal convection was carried out in two aspect-ratio-one convection cells filled with water. Temperature correlation functions and local velocity fluctuations were measured over varying Rayleigh numbers and spatial positions across the entire cell. These measurements fully characterize the spatial structure of the temperature oscillation and reveal the mixing and emission dynamics of the thermal plumes near the conducting surface. A sharp transition from a random chaotic state to a correlated turbulent state of finite coherence time is found when the Rayleigh number becomes larger than a critical value $\mathrm{Ra}_c \simeq 5\times 10^7$. Above Ra_c the measured temperature correlation functions show a well-defined oscillation with a finite coherence time. The oscillation period is found to be twice as large as the cell crossing time. The experiment demonstrates how the thermal plumes in a closed cell organize themselves both in space and time and generate coherent oscillations in a turbulent environment.

DOI: 10.1103/PhysRevE.66.026308 PACS number(s): 47.27.−i, 44.25.+f, 05.40.−a

I. INTRODUCTION

An intriguing feature of turbulent Rayleigh-Bénard convection is the emergence of a well-defined low-frequency oscillation in the temperature power spectrum [1,2]. This oscillation takes place in the hard turbulence regime when the Rayleigh number Ra becomes larger than a critical value $\mathrm{Ra}_c \simeq 5\times 10^7$. Recent velocity measurements [3,4] find a similar oscillation in the velocity power spectrum. The coherent oscillations are observed in various convecting fluids, such as low-temperature helium gas [1,2], mercury [5,6], sulfur hexafluoride gas [3], and water [4,7]. These measurements have stimulated considerable theoretical efforts, aimed at explaining the dynamic origin of the temperature oscillation [1,2,6,8].

It was first interpreted as an oscillation of a stably stratified region of size comparable to the mixing zone [1] and later was linked to the rotation frequency of the large-scale circulation in turbulent convection [2,6]. In the latter case, the oscillation frequency f_0 is determined by the circulation frequency, $U/(4L)$, for an aspect-ratio-one cell with height L and having an average large-scale velocity U. With this interpretation, f_0 has been used to probe U as a function of Ra in low-temperature helium gas [1,2,9,10] and in mercury [5,6]. These two systems are very important for the study of ultrahigh Rayleigh number and ultralow Prandtl number convection, but it is extremely difficult to carry out direct velocity measurements in helium gas and mercury. Finding a reliable velocity indicator from temperature measurements, therefore, becomes essential for the study of turbulent convection in the two systems.

Recently, Villermaux [8] proposed that the temperature oscillation is caused by a thermal boundary layer instability triggered by the incoming thermal plumes, which are transported along the cell periphery by the large-scale circulation. His model assumes that the unstable modes (i.e., the thermal plumes) in the upper and lower thermal boundary layers interact through a delayed nonlinear coupling with a time constant $t_0 \simeq L/U$, which is the transit time for thermal plumes to travel between the two conducting surfaces of the cell (cell crossing time). Because of this delayed coupling, the thermal plumes are excited alternately between the upper and lower boundary layers with a local frequency $f_0 = 1/(2t_0) \simeq U/(2L)$. Villermaux's model provides an interesting mechanism for the temperature oscillation, but its predictions have not been examined experimentally in detail.

In an attempt to further understand the structure and dynamics of the thermal plumes, we have recently carried out a systematic study of the temperature and velocity fields in turbulent convection. Using the techniques of laser Doppler velocimetry (LDV), thermometry, and flow visualization, we map out the temperature and velocity structures in the plane of the large-scale circulation. These temperature and velocity measurements are conducted in convection cells with different aspect ratios and over varying Rayleigh numbers and spatial positions across the cell. Water is used as the convecting fluid, in which the temperature and velocity measurements can be made simultaneously with high accuracy. These local measurements provide a body of reliable velocity and temperature data and complement the global measurements of heat transport in turbulent convection [1,9–13].

In Ref. [14] (and a rapid communication [4]), we have described the detailed structure of the mean velocity field in three different convection cells with the aspect ratio $A = 0.5$, 1, and 2, respectively. Large velocity fluctuations are found both in the central region and near the cell boundary. Despite the large velocity fluctuations, the flow field still maintains a large-scale quasi-two-dimensional structure, which rotates in a coherent manner. An important finding of the experiment is that the spatial distribution of the thermal plumes in a closed cell is neither homogeneous nor isotropic. The thermal plumes organize themselves in such a way that warm plumes accumulate on one side of the cell and cold plumes concentrate on the opposite side of the cell. Because of buoyancy, the spatial separation of warm and cold plumes provides a self-feeding mechanism, which drives the large-scale circulation continuously.

*Email address: ptong@okstate.edu

In this paper, we focus our attention on the structure of the temperature field in turbulent convection. Direct measurements of local temperature fluctuations and their spatial correlation functions are carried out in two aspect-ratio-one cells over varying Rayleigh numbers and spatial positions across the entire cell. These measurements reveal the emission and mixing dynamics of the thermal plumes near the conducting surface and explain the dynamic origin of the temperature oscillation in turbulent convection. The experiment demonstrates that the thermal plumes in a closed cell are organized not only in space but also in time, which provides a unique driving mechanism for the convective flow. It is shown that the structural measurements are essential for the physical understanding of turbulent convection, whereas single-point measurements can only provide limited information.

The remainder of the paper is organized as follows. We first describe the apparatus and the experimental method in Sec. II. Experimental results are discussed in Sec. III. Finally, the work is summarized in Sec. IV.

II. EXPERIMENT

The experiment is conducted in two vertically oriented cylindrical cells filled with water. The height of the larger cell is 19.4 cm and its inner diameter is 19.0 cm. The smaller cell is 8.2 cm in height and 8.2 cm in inner diameter. The corresponding aspect ratio (A=diameter/height) of these cells is unity. Details about the apparatus have been described elsewhere [15], and here we mention only some key points. The sidewall of the cells is made of a transparent Plexiglas ring with a wall thickness of 0.6 cm. The upper and lower plates are made of brass and their surfaces are electroplated with a thin layer of gold. Two silicon rubber film heaters connected in parallel are sandwiched on the backside of the lower plate to provide constant and uniform heating. The upper plate is in contact with a cooling chamber, whose temperature is maintained constant by circulating cold water from a temperature bath. The temperature difference ΔT between the upper and lower plates is measured by two thermistors embedded in each plate.

The two cells are used to extend the accessible range of the Rayleigh number $\mathrm{Ra}=\alpha g \Delta T L^3/(\nu\kappa)$, where g is the gravitational acceleration, L is the cell height, and α, ν, and κ are, respectively, the thermal expansion coefficient, the kinematic viscosity, and the thermal diffusivity of the convecting fluid (water). The larger cell covers the Ra range between 7.5×10^8 and 1×10^{10}, and the smaller cell covers the Ra range between 1.8×10^7 and 7.1×10^8. In the experiment, the mean temperature of the bulk fluid is kept at $\sim$29 °C and the corresponding Prandtl number, $\mathrm{Pr}=\nu/\kappa$, is $\sim$5.5. The temperature of the upper and lower plates is regulated within 0.1 °C in standard deviation, which is less than 2.5% of the maximum ΔT used in the experiment.

Figure 1(a) shows the experimental arrangement for the temperature and velocity measurements. Two small movable thermistors ($T1$ and $T2$) of diameter of 0.2 mm, time constant of 15 ms, and temperature sensitivity of 1 mK/Ω (Thermometrics, AB6E3-B10KA202J) are used to measure the local fluid temperature. To guide the thermistors into the

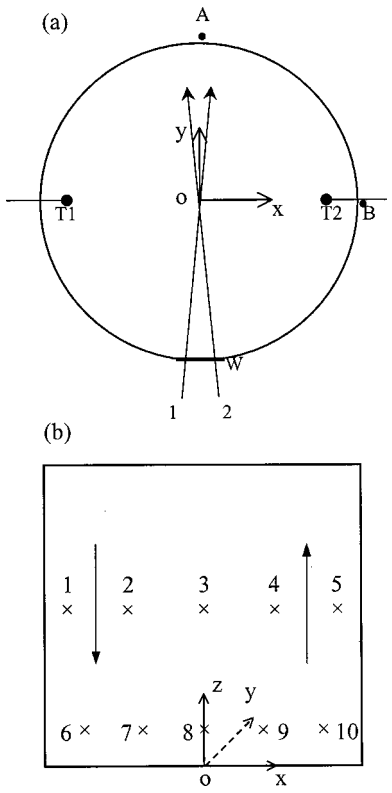

FIG. 1. (a) Schematic diagram of the experimental setup (top view): $T1$, $T2$, temperature probes; 1, 2, laser beams for LDV; W, optical window. (b) Space coordinates and ten locations for the temperature measurements. The long arrows near the sidewall indicate the direction of the large-scale circulation.

cell, we install two horizontal stainless steel tubes of diameter of 1.1 mm on two opposing sides of the sidewall. The two tubes can be mounted at three different heights of the cell. At a given height each tube can slide in and out so that the local fluid temperature $T_i(t)$ (here i is used to indicate the probe position) can be measured at various horizontal positions away from the sidewall. All the thermistors used are calibrated individually with an accuracy of 0.01 °C. Each thermistor is connected to an ac bridge as a resistance arm. The voltage signals from the two ac bridges are measured simultaneously by a two-channel dynamical signal analyzer (HP 35665A) at a sampling rate ranging from 2 to 20 Hz. Smaller sampling rates are used to obtain long-time records (18–36 h) in order to achieve better statistics for low-frequency data. Typically, we take 7-h-long time series data ($\sim4\times10^5$ data points) at each position for the correlation, power spectrum, and Ra-dependence measurements. This data accumulation time is much longer than the time scale for the large-scale circulation, which is of the order of 1 min, ensuring that the statistical average of the flow properties is adequate. In this way, we obtain a complete series of temperature data at various Rayleigh numbers and spatial locations with the highest statistical accuracy possible.

Local velocity measurements are conducted using a two-component LDV system (TSI Inc.) together with an argon-ion laser (Coherent Innova 90). A long rectangular flat window (W) is inserted onto the sidewall to admit the incident

laser beams and observe the scattered light by the seed particles. The width of the optical window is 3 cm for the larger cell and 1.5 cm for the smaller cell and its length is the same as the height of the Plexiglas ring. Two pairs of laser beams of different color (blue and gree) coming from a fiber-optic transceiver of the LDV system are directed through the optical window and focused onto a single measuring point inside the convection cell. The fiber-optic transceiver has a receiving fiber, which collects the scattered light in the backward direction and feeds it to two photomultiplier tubes. The focusing spot has a cylindrical probe volume of 1.31 mm in length and 0.09 mm in diameter. The two laser beams shown in Fig. 1(a) are in the horizontal plane and are used to measure the horizontal velocity v_x in the x direction. The other two laser beams (not shown) are in the vertical plane parallel to the laser propagation direction. These two beams are used to measure the vertical velocity v_z in the z direction.

The analog signals from the photomultiplier tubes are fed to a two-channel LDV signal processor (Model IFA-655, TSI Inc.), which uses the fast Fourier transform to resolve the two velocity components. The sampling rate of the velocity measurements is 10–15 Hz, which is approximately ten times larger than the cutoff frequency of the velocity power spectrum. In the calculation of the velocity statistics, we use the transit time weighting to correct for the velocity sampling bias [16]. Monodisperse polymer latex spheres of 4.75 μm in diameter are used as the seed particles. Because their density (1.05 g/cm^3) matches closely to that of water, the seed particles follow the local flow well. In the experiment, we measure the local velocity as a function of time and the measuring position (laser focusing spot) can be varied continuously along the y axis (horizontal scan) and the z axis (vertical scan). This is accomplished by moving the LDV fiber-optic transceiver probe, which is mounted on a traversable table.

Figure 1(b) shows the space coordinates to be used below in the presentation of the temperature and velocity measurements. The origin of the coordinate system coincides with the center of the lower conducting surface. The x and z axes are in the rotation plane of the large-scale circulation (LSC) and the y axis is perpendicular to the rotation plane. The ten marks indicate the locations of the temperature measurement made in the rotation plane. Early temperature measurements [6] showed that the azimuth of LSC rotates slowly in time when the cylindrical cell is leveled perfectly. To pin down the azimuthal rotation, we tilt the cell with a small angle ($<1°$) by adding a few sheets of paper on one side of the cell bottom. Ciliberto *et al.* [7] have shown that such a small tilt does not affect turbulent convection very much. When we tilt the cell at the position B [see Fig. 1(a)], LSC is set up in the x-z plane and its rotational direction is shown in Fig. 1(b). In this case, the LDV setup shown in Fig. 1(a) is capable of measuring the two in-plane velocity components v_x and v_z. Similarly, we can tilt the cell at the position A. In this case, LSC is set up in the y-z plane and one can measure an in-plane velocity component along the mean flow direction and an out-plane velocity component perpendicular to the rotation plane of LSC. To avoid confusion, hereinafter we choose the x-z plane to coincide with the rotation plane of LSC regardless of the actual arrangement of the tilt.

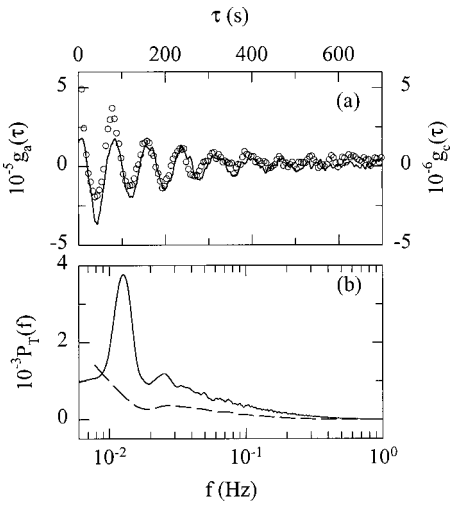

FIG. 2. (a) Measured temperature autocorrelation function $g_a(\tau)$ (open circles) and cross-correlation function $g_c(\tau)$ (solid curve) as a function of delay time τ at Ra$=1.4\times10^9$. (b) Measured frequency power spectra $P_T(f)$ of the temperature signals near the sidewall at Ra$=1.4\times10^9$ (solid curve) and at Ra$=4.7\times10^7$ (dashed curve).

III. RESULTS AND DISCUSSION

A. Spatial structure of temperature oscillations

We first discuss the temperature oscillation in the plane of LSC. Some of the results have been reported previously in a rapid communication [17]. Figure 2(a) shows the measured temperature cross-correlation function, $g_c(\tau) = \langle \delta T_1(t)\, \delta T_5(t+\tau)\rangle/\Delta T^2$, as a function of delay time τ at Ra$=1.4\times10^9$ (solid curve) [18]. Here the temperature fluctuation is defined as $\delta T_i(t) = T_i(t) - \overline{T_i}$, with $\overline{T_i}$ being the local mean temperature. In the experiment, the two temperature probes are placed, respectively, at positions 1 and 5 (both at midheight of the cell and 8 mm away from the sidewall) as indicated in Fig. 1(b). Figure 2(a) reveals two important features of $g_c(\tau)$. First, the measured $g_c(\tau)$ has a well-defined oscillation at f_0, which varies with both L and Ra (see Fig. 12 below). Second, the amplitude of the oscillation decays with time, indicating that the oscillation has a finite coherence time τ_c. These interesting features are also observed in the autocorrelation function, $g_a(\tau) = \langle \delta T_i(t)\, \delta T_i(t+\tau)\rangle/\Delta T^2$ ($i=1$ or 5), as shown by the open circles in Fig. 2(a).

The emergence of a well-defined oscillation in the sidewall region is an intriguing feature of turbulent convection and has stimulated considerable theoretical debates on its dynamic origin [1,2,6]. Villermaux's model [8] provided a detailed description for the temperature oscillation and gave two specific predictions, which can be compared with experiment. The first prediction is about the oscillation pattern of the local temperature signals. Because of the alternating emission of thermal plumes between the upper and lower thermal boundary layers, a local temperature probe at posi-

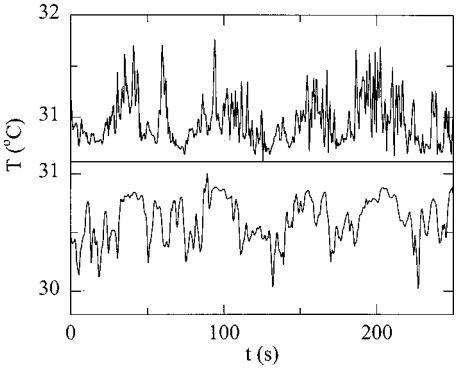

FIG. 3. Time series measurement of temperature fluctuations at position 5 (upper curve) and position 1 (lower curve). The measurements are made at $\mathrm{Ra}=3.2\times10^9$.

tion 5, for example, will detect strong and weak burst signals in alternation. As indicated in Fig. 4 (see the discussion on Fig. 6 for more details), the strong signals come from the rising warm plumes that are generated from the lower conducting surface (at the lower right corner of the cell) when the falling cold plumes hit the lower surface (on the lower left side of the cell). These signals contribute to a dominant peak at f_0 in the frequency power spectrum $P_T(f)$. The weak signals, on the other hand, come from those warm plumes that are produced from the lower surface (at the lower right corner of the cell) when the cold plumes just erupt from the upper surface (at the upper left corner of the cell). Because of buoyancy, the emission of the cold plumes produces a pulsation to the large-scale circulation, which triggers a weak burst of warm plumes at the lower surface. Because the (hydrodynamic) interaction is indirect and long ranged, the impact of the pulsation on the plume emission at the lower surface is weaker when compared with the direct bombardment by the cold plumes. These weak burst signals give rise to a smaller peak at $2f_0$ in $P_T(f)$. Indeed, the measured $P_T(f)$ (solid curve) in Fig. 2(b) clearly reveals a dominant peak at $f_0=0.0117$ Hz and a second peak at $2f_0$. Figure 2 thus confirms the first prediction of Villermaux's model. The small second peak was also observed recently in a low-temperature convection experiment [19].

In fact, the strong temperature oscillations can be observed directly from the time series data. Figure 3 shows the time series measurement of temperature fluctuations at position 1 and position 5. It is seen that the temperature fluctuations in the sidewall region are highly skewed toward one direction. Cold fluctuations are superposed on an average base line at position 1 and warm fluctuations are found at position 5. The downward going spikes are associated with falling cold plumes and the upward going spikes are associated with rising warm plumes. They are separated into two opposing sidewall regions. From the flow visualization at $\mathrm{Ra}\simeq10^9$, we observe that the thermal plumes in the sidewall region often group together when moving across the cell. Individual plumes are observed rarely near the sidewall. This collective behavior of the thermal plumes is clearly seen in Fig. 3(a). They arrive in groups at a frequency f_0 so that a dominant peak is found in $P_T(f)$. Figure 3 thus suggests that the temperature oscillation is generated by a process involving many interacting plumes. We will discuss this effect further in Sec. III B. It is also found from Fig. 3 that the two burst signals at position 1 and position 5 are out of phase. Because the local mean temperature $\overline{T_i}$ is shifted from the average base line (such that $\langle \delta T_i(t)\rangle=0$), on which the burst signals are superposed, the measured $g_c(\tau)$ is shifted upward with a positive value at $\tau=0$ [see Fig. 2(a)].

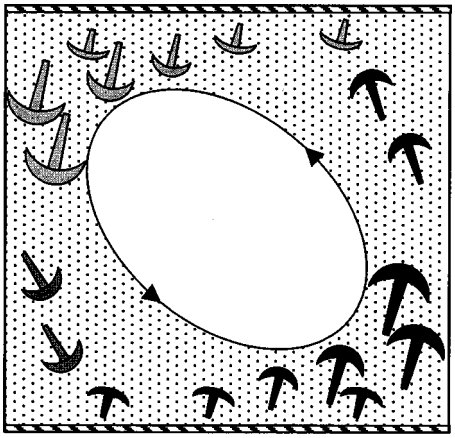

FIG. 4. A schematic drawing of the velocity field and the plume distribution in the aspect-ratio-one cell. The central core region (unshaded) is the fully mixed bulk region and the shaded area shows the plume-dominant region. The thin layers with wiggly lines near the upper and lower surfaces indicate the thermal boundary layers. Cold plumes (light colored) fall on the left side of the cell and warm plumes (dark colored) rise on the right side of the cell. The arrows indicate the direction of the large-scale circulation.

The second prediction of Villermaux's model gives a relationship between the oscillation frequency f_0 and the large-scale velocity U. As mentioned in Introduction, the detailed structure of the velocity field in turbulent convection has been fully documented in Refs. [14,4] and here we only refer to some key points. Figure 4 shows a sketch of the velocity field in an aspect-ratio-one cell. The flow field has a quasi-two-dimensional structure, which undergoes a coherent rotation. The single-roll structure shown in Fig. 4 can be divided into three regions in the rotation plane: (i) a thin viscous boundary layer around the cell periphery, (ii) a fully mixed central core region of size $\sim L/2$, and (iii) an intermediate plume-dominated buffer layer of thickness $\sim L/4$. The plume-dominated buffer layer is the active region that drives the large-scale circulation. Thermal plumes erupt into the region from the upper and lower thermal boundary layers and are separated laterally in the two opposing sidewall regions. The warm and cold plumes exert buoyancy forces on the fluid and drive the vertical rising and falling flows near the sidewall. The central core region is ''sheared'' by the rising and falling plumes near the sidewall, resulting in a constant mean velocity gradient in the region.

With this flow structure, it becomes clear that the nonlinear delay time t_0 in Villermaux's model is the cell crossing time L/U. In Sec. III C we will discuss the measurement of the rotation rate γ of LSC. In the experiment, we obtain γ from the slope of the linear velocity profile in the central core region. The average speed of the large-scale flow near

the sidewall is given by $U \simeq \gamma L/2$. It is shown in Fig. 12 that the normalized oscillation frequency $2f_0L^2/\nu$ (solid triangles) coincides with the Reynolds number $\mathrm{Re}=UL/\nu = \gamma L^2/(2\nu)$ (open circles) in the Ra range between 10^8 and 10^{10}. Figure 12 thus confirms the second prediction, $f_0 = U/(2L)$, of Villermaux's model. Note that the plot in Fig. 12 is a compensated plot, which is sensitive to small variations. The experimental uncertainties for the mean velocity measurement are mainly statistical and the relative error for U is less than 3%. The accuracy of the LDV instrument is better than 1%. We will discuss more experimental details about the large-scale velocity in Sec. III C.

In many early experiments, f_0 was interpreted as the rotation frequency, $U/(4L)$, assuming that the thermal plumes also travel along the upper and lower surfaces with the speed U [2,6]. Figure 12 clearly shows that this is not the case. The important question one might ask is how the temperature disturbances propagate near the conducting surface. Although Villermaux's model explained the main features of the temperature oscillation, it is nevertheless a simplified phenomenological model, which assumes that the interaction between the upper and lower thermal boundary layers can be adequately described by two coupled time-dependent amplitude equations. Because it does not involve any space variables, Villermaux's model cannot provide information about the structure and dynamics of the thermal plumes near the conducting surface. To answer the above question, we measure the temperature fluctuations at five different horizontal locations above the lower surface. The positions 6–10 shown in Fig. 1(b) are 8 mm above the bottom plate (outside the thermal boundary layer) and their horizontal coordinates are, respectively, $x=-8$, -5, 0, 5, and 8 cm. The direction of the horizontal flow near the lower surface is from position 6 to position 10 (left to right).

Figure 5(a) shows the measured cross-correlation functions $g_c(\tau)$ between position 1 and the four horizontal positions 6–9 (top to bottom curves). Using the temperature signal at position 1 as a reference, the cross-correlation functions measure the time required for the thermal plumes to travel from position 1 to the four horizontal positions 6–9. The transit time can be determined by the position of the first peak in the measured $g_c(\tau)$. It is found from Fig. 5(a) that the downward plume traveling time from position 1 to positions 6–9 is, respectively, 12 ± 1, 12 ± 1, 13 ± 2, and 13 ± 2 s. The experimental uncertainties come from the determination of the peak position. If the thermal plumes were carried from position 6 ($x=-8$ cm) to position 9 ($x=5$ cm) by the large-scale flow, the time delay would be $\Delta t=\Delta x/U \simeq 16$ s. Here $U \simeq 0.8$ cm/s is used for the large-scale velocity near the lower surface [14]. The measured time delay is only ~ 1 s, which is much smaller than the calculated Δt. We will discuss the initial phase difference between the top and bottom curves together with Fig. 6.

Similar results are also obtained for the upward plume traveling time. Figure 5(b) shows the measured $g_c(\tau)$ from the three horizontal positions 9–7 to the final position 5 (top to bottom curves). The obtained upward plume traveling time is, respectively, 11 ± 1, 15 ± 2, and 15 ± 2 s. The measured time delay between positions 7 and 9 is 4 ± 2 s, which

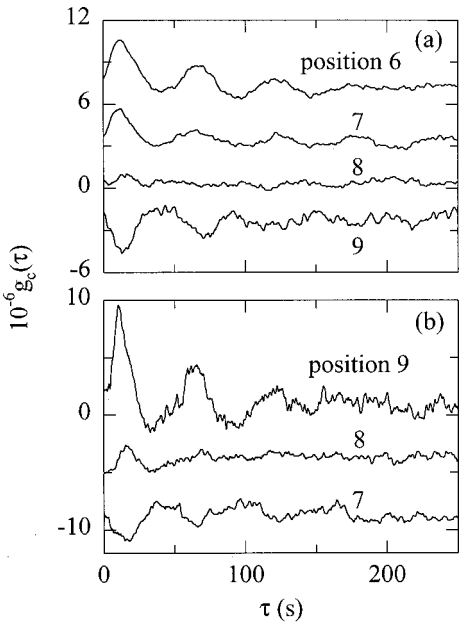

FIG. 5. (a) Measured cross-correlation functions $g_c(\tau)$ between position 1 and the four horizontal positions 6–9 (top to bottom curves). (b) Measured $g_c(\tau)$ from the three horizontal positions 9–7 to the final position 5 (top to bottom curves). All the measurements are made at $\mathrm{Ra}=3.2\times10^9$. For clarity, the origin of each curve is shifted vertically.

is slightly larger than that obtained from Fig. 5(a). While we do not know, at the moment, the detailed dynamics about how such a small time delay is generated, the measurements shown in Fig. 5 clearly support our conclusion that f_0 is determined by $U/(2L)$, rather than $U/(4L)$, and the emission of the thermal plumes over the entire conducting surface is triggered in a time scale much smaller than the cell crossing time L/U.

To further understand how cold plumes are mixed and warm plumes are generated near the lower conducting surface, we compare, in Fig. 6, the local temperature fluctuations at three horizontal positions 6 (upstream), 8 (middle), and 10 (downstream). The upward going spikes shown in Fig. 6 are produced by the warm plumes just erupted from the lower conducting surface. It is seen that the number of newly emitted warm plumes increases toward the downstream direction. In the lower-right corner of the cell (position 10), the warm plumes become very dense and tend to group together.

It has been shown [14] that the velocity field in the lower-left side of the cell is dominated by the downward flow produced by the falling cold plumes. In fact, the measured vertical velocity along the lower central axis of the cell is in the downward direction. The upward flow becomes predominant only in the lower-right corner of the cell, as indicated in Fig. 4. This flow structure together with the temperature measurements shown in Fig. 6 suggest that the heat exchange between the falling cold plumes and the lower conducting surface takes place mainly on the left side of the lower plate ($\sim 3L/4$ in size). Because of strong thermal mixing, the emission of warm plumes is suppressed by the falling cold

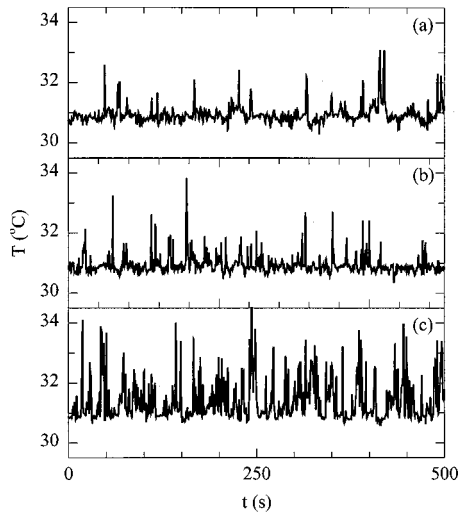

FIG. 6. Time series measurement of temperature fluctuations at positions (a) 6 ($x=-8$ cm), (b) 8 ($x=0$ cm), and (c) 10 ($x=8$ cm). The measurements are made at Ra$=3.2\times10^9$.

plumes in the region. As a result, one sees less warm plumes on the lower-left side of the plate and more warm plumes are observed on the lower-right side ($\sim L/4$ in size). Figure 4 shows a sketch of the spatial distribution of thermal plumes in the aspect-ratio-one cell. This plume distribution explains why the top and bottom curves in Fig. 5(a) [and in Fig. 5(b)] have a different initial phase. Because the cold plumes occupy predominately on the lower-left side of the cell, the measured $g_c(\tau)$ between positions 1 and 6 shows the correlation of the cold plumes traveling across the two positions. At position 9, however, newly emitted warm plumes become predominant and the measured $g_c(\tau)$ in this case shows the correlation between the falling cold plumes at position 1 and the rising warm plumes at position 9. This introduces a negative sign to the measured $g_c(\tau)$.

We also measure $g_c(\tau)$ at other locations in the rotation plane of LSC. The measured $g_c(\tau)$ shows oscillations only when both temperature probes are placed inside the plume-dominated sidewall region. The oscillations disappear from $g_c(\tau)$ when one of the probes is moved out of the region. This is shown in Fig. 7, which displays the measured $g_c(\tau)$ between positions 1 and 3 (solid curve) and between positions 2 and 4 (circles). The three positions 2–4 are all in the central core region with positions 2 and 4 being $\sim L/4$ away from the sidewall (2.2 cm from the sidewall of the smaller cell) and position 3 at the cell center. Inside the sidewall region, maximum correlations are obtained when one of the temperature probes is placed at position 1 and the other is placed at position 5. In this case, one probe detects the rising warm plumes and the other measures the falling cold plumes. The measured $g_c(\tau)$ at other locations in the sidewall region is of the same shape as that shown in Fig. 2(a) but has a different initial phase. This phase difference is consistent with the fact that the fluid moves up on one side the cell and falls down on the opposite side of the cell.

The measured $g_c(\tau)$ also shows oscillations when both temperature probes are placed in the sidewall region but out of the rotation plane of LSC. Figure 8(a) shows the measured

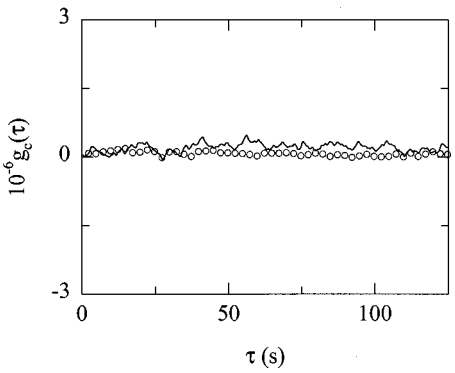

FIG. 7. Measured cross-correlation function $g_c(\tau)$ between positions 1 and 3 (solid curve) and between positions 2 and 4 (circles). The measurements are carried out in the smaller cell at Ra $=7.1\times10^8$.

$g_c(\tau)$ between two sidewall locations, similar to positions 1 and 5 but in the plane perpendicular to the rotation plane of LSC. When compared with Fig. 2(a), we find that $g_c(\tau)$ shown in Fig. 8(a) is always negative and has less oscillation cycles. It is found that the oscillation frequency f_0 is the same as that measured in the rotation plane. To understand the plume motion out of the rotation plane, we plot, in Fig. 8(b), the corresponding temperature fluctuations at the two locations. It is seen that the burst signals are skewed toward one direction only for a short period of time and become symmetric over a longer period of time. This is contrary to the situation in the rotation plane, in which the temperature fluctuations in the sidewall region are locked in one direc-

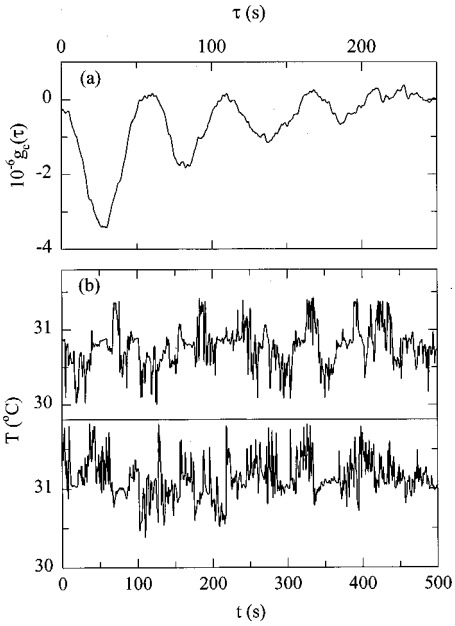

FIG. 8. (a) Measured cross-correlation function $g_c(\tau)$ at Ra $=3.2\times10^9$. In the measurement the two temperature probes are placed in the plane perpendicular to the rotation plane of the large-scale circulation. They are at the midheight of the cell and 8 mm away from the sidewall. (b) Corresponding temperature fluctuations at the two positions.

tion. Careful examination of Fig. 8(b) reveals that the burst signals at the two locations are still correlated and their relative phase is off by π. Because of this π-shift and because the burst signals are superposed on an average base line with zero mean, the final cross-correlation function $g_c(\tau)$ becomes negative at all delay times.

From the above measurements we arrive at the following physical picture for the dynamics of the thermal plumes near the lower conducting surface. When the falling cold plumes arrive at the lower surface, heat exchange takes place in the region occupied by the cold plumes. At (almost) the same time, the impact of the cold plumes triggers off an instability of the lower thermal boundary layer, resulting in an eruption of warm plumes in other regions not occupied by the cold plumes. Because of the strong mixing effect, the emission of warm plumes is suppressed in the region where the falling cold plumes are annihilated. This process gives rise to a spatial separation of cold and warm plumes, which is further enhanced if there exists a stable large-scale flow. Such a flow will localize (or polarize) the spatial arrangement of the cold and warm plumes. Clearly, this is a self-organizing process in that the plume separation and the large-scale flow help each other. In regions where there is not a stable large-scale flow (such as in the plane perpendicular to the rotation plane of LSC), the separation of cold and warm plumes still remains but their spatial arrangement is random in a turbulent environment. In this case, fluctuations become important, which may play an essential role in the random reversal of the large-scale flow when the convection cell is leveled perfectly [6,19].

B. Onset of temperature oscillations

The temperature oscillations discussed above are found only when the Rayleigh number becomes larger than a critical value $\mathrm{Ra}_c \simeq 5\times 10^7$. Below Ra_c the oscillations disappear from the measured $g_c(\tau)$ [and $g_a(\tau)$], and no obvious frequency peak is found in $P_T(f)$ [dashed curve in Fig. 2(b)]. Figure 9(a) shows the measured autocorrelation function $g_a(\tau)$ (solid curve) and cross-correlation function $g_c(\tau)$ (circles) at $\mathrm{Ra}=4.7\times 10^7$ $(<\mathrm{Ra}_c)$. The measured $g_a(\tau)$ becomes a simple decaying function for small values of Ra $(<\mathrm{Ra}_c)$. Figure 9(b) shows the temperature fluctuations at positions 5 (upper curve) and 1 (lower curve) when $\mathrm{Ra}=4.3\times 10^7$. Similar to the situation at large Ra $(>\mathrm{Ra}_c)$, the temperature fluctuations in the sidewall region remain highly skewed toward one direction. Cold fluctuations are superposed on an average base line at position 1 and warm fluctuations are found at position 5. This suggests that the large-scale circulation remains even in the soft turbulence regime $(\mathrm{Ra}<\mathrm{Ra}_c)$. In fact, direct velocity measurements have shown that the velocity profile below Ra_c is approximately of the same shape as that in the hard turbulence regime (see Fig. 4 in Ref. [17]). We therefore conclude that LSC provides only a means to transport the thermal plumes between the two conducting surfaces and is not sufficient to generate the coherent oscillation.

To understand how the coherent oscillation is generated, we examine the coherence time τ_c of $g_c(\tau)$. In the experiment we obtain the value of τ_c by simply counting the number of oscillation cycles through to the noise level of the measured $g_c(\tau)$. For example, we find $\tau_c f_0 \simeq 7$ from Fig. 2(a). Because we are looking at the oscillations with a fixed frequency, the experimental errors for counting the oscillation cycles are not very large. The final uncertainties for $\tau_c f_0$ are ± 1. Figure 10(a) displays the normalized coherence time $\tau_c f_0$ as a function of Ra. It is clearly shown that the mea-

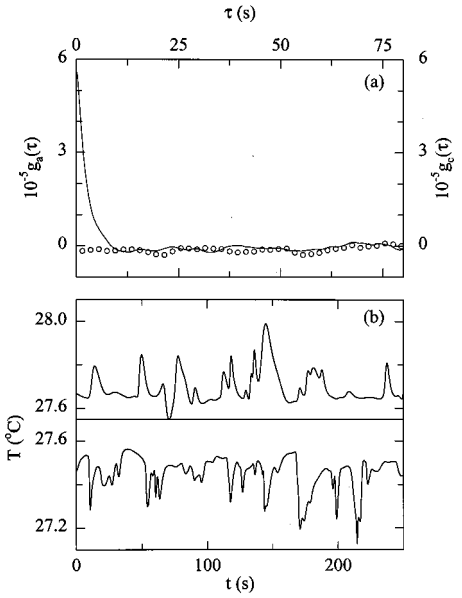

FIG. 9. (a) Measured autocorrelation function $g_a(\tau)$ (solid curve) and cross-correlation function $g_c(\tau)$ (circles) at $\mathrm{Ra}=4.7\times 10^7$. The measurements are conducted in the smaller cell at positions 1 and 5 (5 mm away from the sidewall). (b) Temperature fluctuations at position 5 (upper curve) and position 1 (lower curve). The measurements are made at $\mathrm{Ra}=4.3\times 10^7$.

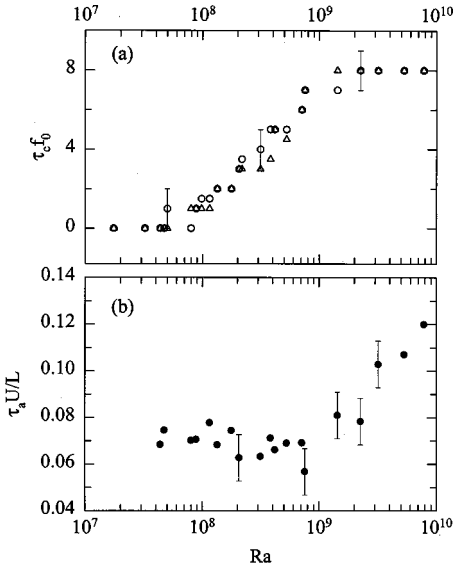

FIG. 10. (a) Normalized coherence time $\tau_c f_0$ as a function of Ra. The circles are obtained from the cross-correlation functions and the triangles are from the autocorrelation functions. (b) Normalized plume size $\tau_a U/L$ as a function of Ra.

sured $\tau_c f_0$ undergoes a transition near $\mathrm{Ra}_c \simeq 5\times10^7$. Below Ra_c the measured $\tau_c f_0$ is zero and no obvious oscillation is found in $g_c(\tau)$. Above Ra_c the measured $g_c(\tau)$ shows oscillations and the coherence time τ_c increases sharply with Ra. At higher values of Ra ($>2\times10^9$), $\tau_c f_0$ becomes saturated at a constant value ~ 8. We notice that the sharp transition for τ_c occurs in the same Ra range as that for the soft-to-hard turbulence transition [1,20]. While various gradual changes between the soft and hard turbulence have been reported in early experiments [1,20,21], Fig. 10(a) reveals a drastic change that occurred near the transition. This is an important finding for the physical understanding of the universal behavior in the hard turbulence regime.

There is a characteristic difference between Fig. 9(b) and Fig. 3. Below Ra_c the thermal plumes arrive individually at random time intervals and no frequency peak is found in $P_T(f)$ [see dashed curve in Fig. 2(b)]. Because of random dephasing, coherent oscillation cannot take place when the rising (or falling) plumes arrive at the upper (lower) surface randomly in time. Therefore, the sharp transition near Ra_c reflects a change of the convective flow from a random chaotic state to a correlated turbulent state of finite coherence time. As shown in Fig. 3, above Ra_c the thermal plumes in the sidewall region tend to group together, indicating that the coherent oscillation involves many interacting plumes. It should be pointed out that the sharp transition near Ra_c is a new effect, which is not included in Villermaux's model. It is assumed in Villermaux's model that the coupling time t_0 between the upper and lower boundary layers is a constant at all values of Ra. As a result, the calculated temperature oscillation has an infinite coherence time. In real turbulent convection, however, t_0 is actually a fluctuating quantity, which will broaden the frequency peak at f_0, or equivalently, shorten the coherence time of the measured $g_c(\tau)$ [8].

From Fig. 2(a) we find that the cell crossing time is $t_0 = 1/(2f_0) \simeq 42.7$ s at $\mathrm{Ra} = 1.4\times10^9$. This time is too long for an individual rising plume of life time $t_1 \simeq \delta^2/\kappa$ to reach the upper surface. Here we take the thermal boundary layer thickness δ as the characteristic length (i.e., the thickness) of the plume. Using the experimental values $\delta \simeq 1.27$ mm and $\kappa \simeq 1.47\times10^{-3}$ cm^2/s, we have $t_1 \simeq 11$ s. This estimate suggests that above Ra_c the rising and falling plumes in the sidewall region must be a new class of plumes, whose lifetime is longer than δ^2/κ. For example, if two thermal plumes combine to form a ''composite plume,'' the plume size is doubled and thus its lifetime is quadrupled. In this case, we have $t_2 \simeq (2\delta)^2/\kappa \simeq 44$ s, which is very close to the cell crossing time t_0.

In fact, one can be obtain the plume size directly from the decay time τ_a of the measured $g_a(\tau)$ shown in Fig. 9(a). Physically, τ_a represents the typical duration of the fluctuating signals shown in Fig. 9(b). Therefore, we have $\tau_a \simeq \delta_a/U$, where δ_a is a characteristic (''vertical'') size of the thermal plumes passing through the temperature probe with a speed U. Figure 10(b) shows the normalized (''vertical'') plume size $\delta_a/L = \tau_a U/L$ as a function of Ra. The decay time τ_a is obtained from the exponential fit to the initial decay of the measured $g_a(\tau)$. It is found that the exponential-like decay of $g_a(\tau)$ persists even when $\mathrm{Ra} > \mathrm{Ra}_c$. The flow velocity used is $U \simeq \gamma L/2 = 3.0\times10^{-5}\ \mathrm{Ra}^{0.46}$ cm/s, where γ is the measured rotation rate of LSC. As shown in Fig. 12 below, this power law describes the velocity data well for $\mathrm{Ra} > 5\times10^8$ but has relatively larger uncertainties for lower values of Ra. As a result, the data shown in Fig. 10(b) exhibit somewhat larger scatterers at the lower values of Ra. Nevertheless, Fig. 10(b) clearly shows that δ_a is almost doubled as Ra is increased from $\sim 5\times10^8$ to $\sim 1\times10^{10}$. Figure 10(b) thus provides an important evidence for the formation of composite plumes.

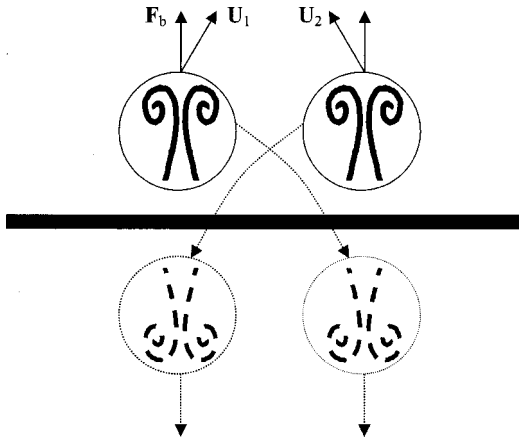

FIG. 11. A schematic drawing of two nearby warm plumes (solid images) forced away from the lower conducting surface by the buoyancy force F_b. They are drawn together by the hydrodynamic interactions, because the flow due to one plume's image force (dashed images) pulls the other plume towards it.

It should be noted that the thermal plume is an anisotropic object with its vertical size being much larger than its horizontal width. As shown in Fig. 10(b), the normalized (vertical) plume size is $\delta_a/L \simeq 0.07$ at $\mathrm{Ra} = 1\times10^8$, which is approximately five times larger than the corresponding thermal boundary layer thickness $\delta/L \simeq 0.014$. We also find that the measured τ_a near the lower surface at positions 6, 8, and 10 (not shown) is, on average, three times smaller than that measured near the sidewall. Because the measured τ_a near the lower surface is proportional to the horizontal width of the thermal plumes (which pass through the temperature probe with a horizontal speed U), this result suggests that the characteristic width of the thermal plumes is indeed comparable to the thermal boundary layer thickness.

From the above measurements we conclude that at lower Ra ($<\mathrm{Ra}_c$), only a small number of thermal plumes is generated near the conducting surfaces. These plumes erupt from the thermal boundary layers randomly and move independently in the convection cell. More plumes are generated as Ra increases, and the system becomes ''concentrated'' when $\mathrm{Ra} > \mathrm{Ra}_c$. In this case, the thermal plumes start to interact through the flow field generated by themselves. Figure 11 shows a possible mechanism for the generation of a ''hydrodynamic attraction'' between two rising (or falling) plumes near the conducting surface. The two nearby warm plumes in Fig. 11 (solid images) are pushed away from the lower conducting surface by the buoyancy force F_b. The

flow field generated by the two rising plumes must vanish on the lower surface, which can be achieved by introducing two downward going image plumes (dashed images), similar to image charges used in electrostatics. As shown in Fig. 11, the flow field from one plume's image tends to pull the other plume towards it, and vice versa. This problem has been solved analytically for two rising solid spheres near a substrate [22] and we believe that the same principle is also applicable to the thermal plumes near the conducting surface. With this ''hydrodynamic attraction,'' the motion of the rising plumes becomes correlated in time. This correlated motion provides synchronized stimulations, which are needed for the generation of the coherent oscillation.

It should be pointed out that the argument given in Fig. 11 for the plume attraction is based on the assumption that the flow field generated by a plume is similar to that of a solid sphere (a long-ranged monopole field). There will be neither attraction nor repulsion for two rising spheres at low Reynolds numbers when they are far away from the boundary. This is because the Stokes equation for the two rising spheres is invariant when the direction of all the velocities and forces is reversed [23]. Moses *et al.* have shown [24,25] that the flow field generated by a laminar plume in a quiescent background can be adequately described by a dipolelike velocity potential. Two such rising laminar plumes are found to attract and coalesce when their separation becomes smaller than the size of the plumes. If this result could be applied to turbulent convection, one would expect that the two rising plumes shown in Fig. 11 will remain attractive even when they move to the sidewall region.

However, the interaction between the thermal plumes in turbulent convection is more complicated and has not been explored in detail. First, the attraction between two laminar plumes is obtained in a quiescent background. In turbulent convection, however, the dense rising (or falling) plumes in the sidewall region entrain the surrounding fluid in such a way that the fluid velocity becomes comparable to that of the plumes. Second, the thermal plumes themselves may become turbulent at high Rayleigh numbers. In fact, we have found in a flow visualization [15] that the cap size of a starting plume near the lower conducting surface is $d_p \simeq 3.4$ cm at $\mathrm{Ra}=2.6\times10^9$. Given the large-scale velocity $U\simeq 0.8$ cm/s, we have $\mathrm{Re}_p = U d_p/\nu \simeq 270$. This Reynolds number based on the cap size is larger than the transition Reynolds number $\mathrm{Re}_c \simeq 220$, above which thermal plumes lose their stability [26]. Clearly, the interaction between the thermal plumes is an essential ingredient for describing the velocity and temperature structures in turbulent convection and needs to be further studied.

C. Rayleigh number dependence

It has been shown [14] that the maximum mean velocity in the aspect-ratio-one cell is located in the plume-dominated buffer layer around the cell periphery. In the central core region, the measured rotational velocity $\overline{u}$ is well described by a linear function of radial distance r away from the cell center. The slope γ of the straight line for $\overline{u}$ remains the same in both the vertical scan across the cell height and the horizontal scan across the cell diameter. This suggests that the bulk fluid indeed undergoes a two-dimensional rotation around the cell center. From the measured γ we define a characteristic large-scale velocity $U=\gamma L/2$ and the corresponding Reynolds number is given by $\mathrm{Re}=UL/\nu = \gamma L^2/(2\nu)$. Figure 12 shows the Rayleigh number dependence of the measured Re. To view deviations from the $\mathrm{Ra}^{0.5}$ scaling more clearly, we plot the data in logarithmic scales with $\mathrm{Ra}^{0.5}$ being divided out. The velocity measurements are conducted in both aspect-ratio-one cells and the data points for $\mathrm{Ra}>7\times10^8$ are obtained from the larger cell.

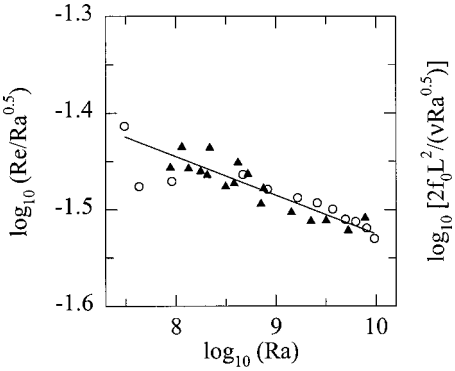

FIG. 12. Measured $\mathrm{Re}/\mathrm{Ra}^{0.5}$ (circles) and normalized oscillation frequency $(2f_0L^2/\nu)/\mathrm{Ra}^{0.5}$ (solid triangles) as a function of Ra. The measurements are conducted in two aspect-ratio-one cells and f_0 is obtained from the temperature power spectrum measured near the sidewall. The solid line is a power-law fit $\mathrm{Re}=0.075\ \mathrm{Ra}^{0.46}$ to all the data points.

In the velocity profile measurements, we measure the local velocity over varying locations and each data point is averaged over 2 h. The rotation rate γ is obtained from the linear profile with more than ten data points evenly spaced across the central region of size $\sim L/2$. Therefore, the data points shown in Fig. 12 have been averaged many times and represent the best set of velocity data we have to date. The three data points in the Ra range between 5×10^7 are 1×10^8 are obtained in the smaller cell. This set of data shows a somewhat larger scatterer, because the flow in the smaller cell is slower and the final statistical average is not as large as that for the larger-cell data. It is seen that the velocity data are well described by an effective power law $\mathrm{Re}=0.075\ \mathrm{Ra}^{0.46}$ (solid line).

As discussed in Sec. III A, the oscillation frequency f_0 is related to the large-scale flow via $f_0 \simeq U/(2L)$. The solid triangles in Fig. 12 are the normalized oscillation frequency $2f_0L^2/\nu$ measured in the Ra range between 10^8 and 10^{10}. It is seen that the two sets of data coincide with each other, suggesting that the oscillation period $1/f_0$ is indeed twice as large as the cell crossing time $t_0=L/U$. For convection experiments in helium and mercury, direct velocity measurements are extremely difficult. The results shown in Fig. 12 thus provide an important connection between the temperature and velocity measurements in turbulent convection.

While the fitted power-law exponent of 0.46 is close to the classical value of 0.5 for the free-fall velocity [2,6,19], Fig. 12 clearly shows that the difference between the two

TABLE I. Experimental results for the normalized large-scale velocity, $U_1 L/\kappa \sim \mathrm{Ra}^{\beta}$, near the sidewall.

β values	Pr range	Technique used	References
0.485	0.64–1.4 (helium)	Dual thermometer	[1,2]
0.488	0.7 (helium)	Dual thermometer	[9]
0.50	~0.7 (helium)	Dual thermometer	[19]
0.50	~5.5 (water)	Dual laser beam	[30]
0.46	0.024 (mercury)	Dual thermometer	[5]

values is beyond the experimental uncertainties. This small difference in exponent can be explained by a recent theoretical model proposed by Grossmann and Lohse (GL) [27]. Within the GL theory, the origin of having an effective exponent less than 0.5 comes from the combined contributions from several dynamic regimes, in which the boundary layer and bulk contributions to the kinetic and thermal dissipations have different scaling exponents [28]. Although the measured exponent is clearly smaller than 0.5, one should interpret the result with caution, especially when the control parameter Ra is varied only in a limited range. In recent years, the large-scale flow in turbulent convection has been measured using various velocimetry methods [14]. These measurements showed that the large-scale velocity U can be adequately described by a common power law, $U \sim \mathrm{Ra}^{\beta}$, but the measured exponent β varies among the experiments in a range between 0.5 and 0.42, which is comparable to the small difference discussed above.

To understand the small variations in β, we need to examine the exact sampling conditions, under which the velocity measurements are performed. Up to now one has measured three different kinds of large-scale velocity in the aspect-ratio-one cell: (1) the maximum local mean vertical velocity U_1 near the sidewall, (2) the maximum linear velocity, $U_2 = \gamma L/2$, determined from the mean rotation rate γ, and (3) a spatially averaged large-scale velocity, $U_3 = 2 f_0 L$, determined from the temperature (or velocity) oscillation frequency f_0. In a recent experiment [29], we have found that the temperature and velocity oscillations have the same frequency f_0. The velocimetry methods used in these experiments have different sensitivities to velocity fluctuations in turbulent convection. Some techniques are sensitive only to the large velocity fluctuations associated with strong thermal plumes and others can pick up smaller fluctuations as well [14]. Consequently, the mean velocities obtained in these experiments are averaged over somewhat different ensembles.

Most measurements of U_1 in the sidewall region were performed using a dual-thermometer setup [2]. By measuring the cross-correlation function between two temperature signals, one obtains the average transit time of large temperature fluctuations (e.g., thermal plumes) across two nearby temperature probes. The flow velocity is determined by the distance between the two probes divided by the measured transit time. Like many time-of-flight velocimeters, the dual-thermometer method has a cutoff velocity and thus is insensitive to small velocity fluctuations [14]. As shown in Table I, the measurements of U_1 give consistent results with $\beta = 0.5$ for helium gas ($\mathrm{Pr} \simeq 0.7$) and water ($\mathrm{Pr} \simeq 5.5$) and

TABLE II. Experimental results for the normalized oscillation frequency, $2 f_0 L^2/\kappa \sim \mathrm{Ra}^{\beta}$.

β values	Pr range	References
0.49	0.64–1.4 (helium)	[1]
0.47	~0.7 (helium)	[19]
0.46	~5.5 (water)	Present expt.
0.43	1–93 (SF_6)	[3]
0.46	0.024 (mercury)	[5]
0.424	0.024 (mercury)	[6]
0.42	3–7 (water)	[31]
0.43	3–1027 (solvents)	[32]

$\beta = 0.46$ for mercury ($\mathrm{Pr} \simeq 0.024$). Because the bulk fluid temperature was not kept constant in some of the velocity measurements, converting Péclet number, $\mathrm{Pe} = U_1 L/\kappa$, to Reynolds number, $\mathrm{Re} = U_1 L/\nu$, results in small changes in β [19]. This is partially due to the fact that the large-scale flow also depends strongly on Pr [3,9]. It is difficult to compare the amplitude of the obtained power laws, because the velocity measurements were conducted in leveled convection cells, in which the azimuth of LSC rotates slowly in time [6]. Therefore, these velocity measurements were not made at the same location relative to LSC. Recently, we measured U_1 using LDV in a tilted cell, in which the rotation plane of LSC is fixed. We conducted the velocity measurements at three values of Ra and found that U_1 is ~22% larger than U_2 [14].

Table II summarizes the measurements of U_3 $(= 2 f_0 L)$ in various convecting fluids. It is seen that the values of β obtained vary slightly among the experiments with a typical value 0.46 ± 0.03. We notice that those velocity measurements that are more sensitive to the large persistent thermal plumes near the sidewall tend to give an exponent $\beta = 0.5$, whereas the other velocity measurements involving more "bulk average" give a smaller value of β. As indicated in Fig. 4, the spatial distribution of the thermal plumes in a closed cell is not uniform and these plumes may have different fate. Some plumes have a short lifetime and are mixed in the bulk region where thermal dissipation is strong. Other plumes group together and accumulate in the sidewall region where thermal dissipation is relatively weak. The "composite plumes" have a longer lifetime and hence are more "ballistic" with a terminal velocity proportional to the free-fall velocity, $U_f = (\alpha g \Delta T L)^{1/2}$. In this case, we have $\beta = 0.5$. Because of strong thermal dissipation, the velocity field in the bulk region may have a different scaling with Ra. Consequently, the Ra-dependence of U_2 and U_3, which involve more bulk average, may have a slightly different exponent β. This conclusion is also supported by recent numerical results [33]. A similar argument could also be made on the mercury system in which (molecular) thermal dissipation is very strong. Further experiments are needed in order to understand the spatial organization of the thermal plumes and explain the small variation in β.

IV. SUMMARY

We have carried out a systematic study of the temperature field in turbulent thermal convection. Direct measurements

of local temperature fluctuations and their correlation functions were conducted in two aspect-ratio-one cells with varying Rayleigh numbers and spatial positions across the entire cell. These measurements fully characterize the spatial structure of the temperature oscillation and reveal the mixing and emission dynamics of the thermal plumes near the conducting surface. A sharp transition from a random chaotic state to a correlated turbulent state of finite coherence time is found when the Rayleigh number becomes larger than a critical value $\mathrm{Ra}_c \simeq 5\times 10^7$. Above Ra_c the measured temperature correlation functions show a well-defined oscillation with a finite coherence time. The oscillation period is found to be twice as large as the transit time for thermal plumes to travel between the two conducting surfaces of the cell (cell crossing time).

With these structural measurements, we now have a complete physical picture for the temperature oscillation in turbulent convection. The temperature oscillation is generated by the alternating emission of cold and warm plumes between the upper and lower thermal boundary layers. These thermal plumes exert vertical buoyancy forces to the bulk fluid. An alternating eruption of thermal plumes, therefore, gives rise to a periodic impulsive force to the fluid. Because the cold and warm plumes are separated laterally into two opposing sidewall regions, the vertical thermal forcing results in a periodic impulsive torque, which drives the large-scale circulation continuously. The central core region is ''sheared'' by the rising and falling plumes near the sidewall, producing a constant mean velocity gradient in the region. Velocity fluctuations in the central region are approximately homogeneous and they are strong enough to fully mix most of the thermal plumes in the region.

Two important conditions must be satisfied in order to generate the coherent temperature oscillation. The first condition is the spatial separation of cold and warm plumes in the convection cell, which is needed in order to set up a large-scale flow. When the falling cold plumes arrive at the lower surface, heat exchange takes place in the region that they occupy. At (almost) the same time, the impact of the cold plumes triggers off an instability of the lower thermal boundary layer, resulting in an eruption of warm plumes in other regions not occupied by the cold plumes. Because of strong thermal mixing, the emission of warm plumes is suppressed in the region where the falling cold plumes are annihilated. This dynamic process provides a basic mechanism for the plume separation near the conducting surfaces. The plume separation is further enhanced by the large-scale circulation, which localizes (or polarizes) the spatial arrangement of the cold and warm plumes in the cell. This is a self-organizing process in that the plume separation and the large-scale flow help each other.

Besides the spatial separation, the thermal plumes are also organized in time to produce synchronized stimulations. This is the second condition required for the generation of the coherent oscillation. As Ra increases, more thermal plumes are generated near the conducting surface and they start to interact through the flow field generated by themselves. Figure 11 illustrates a possible mechanism for the generation of a ''hydrodynamic attraction'' between two rising plumes near the conducting surface. When a warm plume is pushed away from the lower surface by buoyancy, it entrains the surrounding fluid and pulls the nearby plumes towards it. This hydrodynamic attraction allows the warm plumes to move up together and provide a synchronized stimulation to trigger off an instability of the upper thermal boundary layer. It is found that such a temporal organization occurs when the Rayleigh number becomes larger than a critical value $\mathrm{Ra}_c \simeq 5\times 10^7$, which is in the same Ra range as that for the soft-to-hard turbulence transition. The experiment thus provides a unique example to show how the thermal plumes in a closed convection cell organize themselves both in space and time and generate coherent oscillations in a turbulent environment.

ACKNOWLEDGMENTS

We thank L. Kadanoff, S. Grossmann, D. Lohse, K. Sreenivasan, J. Niemela, K.-Q. Xia, E. Ching, and T. Squires for useful discussions. The assistance of M. Lucas and his team in fabricating the convection cells is gratefully acknowledged. This work was supported by the National Science Foundation under Grant No. DMR-0071323.

[1] B. Castaing, G. Gunaratne, F. Heslot, L. Kadanoff, A. Libchaber, S. Thomae, X.-Z. Wu, S. Zaleski, and G. Zanetti, J. Fluid Mech. **204**, 1 (1989).
[2] M. Sano, X.-Z. Wu, and A. Libchaber, Phys. Rev. A **40**, 6421 (1989).
[3] S. Ashkenazi and V. Steinberg, Phys. Rev. Lett. **83**, 3641 (1999); **83**, 4760 (1999).
[4] X.-L. Qiu, S. H. Yao, and P. Tong, Phys. Rev. E **61**, R6075 (2000).
[5] T. Takeshita, T. Segawa, J. A. Glazier, and M. Sano, Phys. Rev. Lett. **76**, 1465 (1996).
[6] S. Cioni, S. Ciliberto, and J. Sommeria, J. Fluid Mech. **335**, 111 (1997).
[7] S. Ciliberto, S. Cioni, and C. Laroche, Phys. Rev. E **54**, R5901 (1996).
[8] E. Villermaux, Phys. Rev. Lett. **75**, 4618 (1995).
[9] X. Chavanne, F. Chilla, B. Castaing, B. Hebral, B. Chabaud, and J. Chaussy, Phys. Rev. Lett. **79**, 3648 (1997); X. Chavanne, F. Chilla, B. Chabaud, B. Castaing, and B. Hebral, Phys. Fluids **13**, 1300 (2001).
[10] J. J. Niemela, L. Skrbek, K. R. Sreenivasan, and R. J. Donnelly, Nature (London) **404**, 837 (2000).
[11] X. Xu, K. M. Bajaj, and G. Ahlers, Phys. Rev. Lett. **84**, 4357 (2000).
[12] G. Ahlers and X. Xu, Phys. Rev. Lett. **86**, 3320 (2001).
[13] K.-Q. Xia, S. Lam, and S.-Q. Zhou, Phys. Rev. Lett. **88**, 064501 (2002).
[14] X.-L. Qiu and P. Tong, Phys. Rev. E **64**, 036304 (2001).
[15] Y.-B. Du and P. Tong, J. Fluid Mech. **407**, 57 (2000).
[16] L. E. Drain, *The Laser Doppler Technique* (Wiley, New York, 1980).

[17] X.-L. Qiu and P. Tong, Phys. Rev. Lett. **87**, 094501 (2001).
[18] The temperature correlation functions shown in Ref. [17] were actually not normalized by the temperature difference ΔT.
[19] J. J. Niemela, L. Skrbek, K. R. Sreenivasan, and R. J. Donnelly, J. Fluid Mech. **449**, 169 (2001).
[20] F. Heslot, B. Castaing, and A. Libchaber, Phys. Rev. A **36**, 5870 (1987).
[21] T. H. Solomon and J. P. Gollub, Phys. Rev. Lett. **64**, 2382 (1990); Phys. Rev. A **43**, 6683 (1991).
[22] T. M. Squires and M. P. Brenner, Phys. Rev. Lett. **85**, 4976 (2000).
[23] P. M. Chaikin, in *Soft and Fragile Matter*, edited by M. E. Cates and M. R. Evans (Institute of Physics Publishing, London, 2000), p. 315.
[24] E. Moses, G. Zocchi, I. Procaccia, and A. Libchaber, Europhys. Lett. **14**, 55 (1991).
[25] E. Moses, G. Zocchi, and A. Libchaber, J. Fluid Mech. **251**, 581 (1993).
[26] D. J. Shlien, Phys. Fluids **21**, 2154 (1978).
[27] S. Grossmann and D. Lohse, J. Fluid Mech. **407**, 27 (2000).
[28] S. Grossmann and D. Lohse, Phys. Rev. E **66**, 016305 (2002).
[29] X.-L. Qiu, X.-D. Shang, P. Tong, and K.-Q. Xia (unpublished).
[30] X.-L. Qiu and K.-Q. Xia, Phys. Rev. E **58**, 486 (1998).
[31] X.-D. Shang and K.-Q. Xia, Phys. Rev. E **64**, 065301 (2001).
[32] S. Lam, X.-D. Shang, S.-Q. Zhou, and K.-Q. Xia, Phys. Rev. E **65**, 066306 (2002).
[33] R.M. Kerr, Phys. Rev. Lett. **87**, 244502 (2001).